

Check for updates

# A Versatile Self-Templating Approach for Constructing **Ternary Halide Perovskite Heterojunctions to Achieve** Concurrent Enhancement in Photocatalytic CO<sub>2</sub> Reduction **Activity and Stability**

Meng-Ran Zhang, You-Xiang Feng,\* Zhao-Lei Liu, Ke Su, Su-Xian Yuan, Min Zhang,\* and Tong-Bu Lu\*

Metal halide perovskite (MHP)-based photocatalysts encounter significant stability challenges in water-containing systems, posing a major obstacle to their application in artificial photosynthesis. Herein, an innovative and universal strategy is present to create MHP-based ternary heterojunctions based on a self-templating method. A series of composite catalysts featuring sandwich hollow structures are constructed, with MHPs such as CsPbBr<sub>3</sub>, Cs<sub>3</sub>Bi<sub>2</sub>I<sub>9</sub>, Cs<sub>3</sub>Sb<sub>2</sub>Br<sub>9</sub>, and Cs<sub>2</sub>AgBiBr<sub>6</sub> serving as the intermediate layers. The unique sandwich structure effectively shields MHPs from direct water contact, allowing MHP-based photocatalysts to exhibit exceptional stability in water-containing photocatalytic environments for durations exceeding 200 h. Furthermore, the hollow design ensures complete contact between the reaction substrates with both the oxidation and reduction functional areas. Compared to single perovskite materials, MHP-based ternary heterojunction photocatalysts exhibit stronger oxidation capability and improved charge separation efficiency, leading to a substantial enhancement in photocatalytic CO2 reduction performance. Notably, the ternary heterojunction with CsPbBr<sub>3</sub> as the intermediate layer achieves an electron consumption rate of up to 1824 µmol g<sup>-1</sup> h<sup>-1</sup> for CO<sub>2</sub> reduction, which is far superior to other reported MHP-based catalysts under similar conditions. This study provides a potent strategy for simultaneously enhancing the stability and activity of MHP-based photocatalysts, paving the way for their potential applications in artificial photosynthesis.

1. Introduction

Mimicking natural photosynthesis to convert CO2 and H2O into high-value chemicals and O2 represents a pivotal pathway

M.-R. Zhang, Y.-X. Feng, Z.-L. Liu, K. Su, S.-X. Yuan, M. Zhang, T.-B. Lu MOE International Joint Laboratory of Materials Microstructure Institute for New Energy Materials and Low Carbon Technologies School of Materials Science and Engineering

Tianjin University of Technology

Tianjin 300384, China

E-mail: youxiangfeng@email.tjut.edu.cn; zm2016@email.tjut.edu.cn; lutongbu@tjut.edu.cn



The ORCID identification number(s) for the author(s) of this article can be found under https://doi.org/10.1002/adfm.202423656

DOI: 10.1002/adfm.202423656

for mitigating the energy crisis and fostering sustainable development.[1,2] In this process, the inherent chemical inertia of CO<sub>2</sub> and the sluggish kinetics of H<sub>2</sub>O oxidation necessitate photocatalysts with robust light-harvesting capabilities and long carrier lifetimes.[3,4] However, most of the developed photocatalysts exhibit limited lightharvesting abilities, [5] and their carrier lifetimes, which are measured in nanoseconds or even picoseconds, [6] are insufficient for enabling long-range transport and efficient utilization of photogenerated carriers.[7] Recently, metal halide perovskites (MHPs), characterized by exceptional photophysical properties,[8] have emerged as potential research hotspots in the development of high-performance artificial photosynthesis catalysts.[9,10] Nevertheless, the ionic nature of MHPs introduces inherent instability under high polarity conditions,[11,12] posing considerable challenges for the construction of artificial photosynthesis systems in aqueous-rich environments.[13,14] Additionally, MHPs suffer from a lack of sufficient catalytic active sites[15] and limited CO2 adsorption capabilities,[16] which further hinder their efficiency in photocatalytic

Therefore, overcoming these obstacles to reactions. fully harness the potential of MHPs is crucial for advancing their application in the field of artificial photosynthesis.

To tackle the aforementioned challenges, MHPs are often safeguarded by constructing core-shell structures[17-19] and adopting spatial confinement strategies.<sup>[20–22]</sup> Although these methods successfully boost the stability and carrier separation efficiency of MHP-based catalysts, they suffer from limited reaction activity due to the restricted accessibility between the inner layer and the reactant substrates. To date, there are still very few examples of efficient and stable MHP-based photocatalysts. Inspired by the layered structure of MHP-based solar cells, [23-26] we have attempted to devise a sandwich-structured MHP ternary heterojunction recently, with lead-free Cs<sub>3</sub>Bi<sub>2</sub>I<sub>9</sub> serving as the core www.advancedsciencenews.com



16163038, O. Downloaded from https://advanced.onlinelbbary.wiley.com/doi/10.1002/adfm.20242356 by Taajii University Of, Wiley Online Library on [03.022025]. See the Terms and Conditions (https://onlinelbbary.wiley.com/terms-and-conditions) on Wiley Online Library for rules of uses; OA aristles are governed by the applicable Creative Commons License

www.afm-journal.de

light-harvesting layer, flanked by semiconductors dedicated to  $\rm H_2O$  oxidation and  $\rm CO_2$  reduction, respectively. As anticipated, the resultant  $\rm TiO_2/Cs_3Bi_2I_9/g\text{-}C_3N_4$  ternary heterojunction  $^{[27]}$  achieved synchronous improvements in photocatalytic activity and stability. However, the sacrificial templating method employed in this preparation process requires strongly corrosive or alkaline reagents for template removal,  $^{[28,29]}$  which can easily lead to the dissociation of amphoteric metal oxides (such as  $\rm Sb_2O_3$  and PbO) that act as intermediates of MHP synthesis (Figure S1, Supporting Information). Therefore, exploring a more universal and mild strategy for constructing MHP-based ternary heterojunctions is crucial for advancing the extensive application of MHPs in the field of artificial photosynthesis.

Herein, inspired by the spontaneous formation of unique hollow structures derived from metal-organic frameworks (MOFs) after calcination (Figure S2, Supporting Information),[30-32] we introduce an universal strategy for constructing ternary heterostructures based on the self-templating method. Initially, the MOF (MIL-125-NH<sub>2</sub>) serves as a template for the in situ growth of a layer of MHP intermediate on its surface. Following calcination, MIL-125-NH<sub>2</sub> is converted into hollow TiO<sub>2</sub>, serving as the oxidation unit. Subsequently, graphdiyne (GDY) is grown in situ on the surface of the MHP intermediate, functioning as the reduction unit. Ultimately, the intermediate layer is converted into MHP, achieving the construction of the ternary heterojunction. This approach avoids the extreme chemical environments required by the sacrificial templating method, and effectively protects the MHP intermediate. Furthermore, the ternary heterojunction system facilitates the creation of dual built-in electric fields, enabling rapid separation and transport of carriers. Experimental findings reveal that all the MHP-based photocatalysts  $(TiO_2/MHP/GDY, with MHP = CsPbBr_3, Cs_3Bi_2I_9, Cs_3Sb_2Br_9, or$ Cs<sub>2</sub>AgBiBr<sub>6</sub>) prepared via the self-templating method exhibit exceptional photocatalytic activity and stability, showcasing the immense potential of this strategy in enhancing the activity and stability of MHP-based photocatalysts. Notably, the ternary heterojunction based on CsPbBr<sub>3</sub> achieves an unprecedented electron consumption rate of 1825 µmol g<sup>-1</sup> h<sup>-1</sup> for photocatalytic CO<sub>2</sub> reduction, while maintaining stability exceeding 200 h in watercontaining systems.

#### 2. Results and Discussion

## 2.1. Preparation and Characterization of TiO<sub>2</sub>/MHP/GDY Ternary Heterojunction

All ternary heterojunctions were prepared by the self-templating method combined with sequential deposition technology, as outlined in the Experimental Section. Considering  $TiO_2/CsPbBr_3/GDY$  as an representative example (**Figure 1a**), the process began with the synthesis of the MIL-125-NH<sub>2</sub> template via a solvothermal method.<sup>[33]</sup> Zeta potential measurement confirmed that its surface carries a negative charge of -26.45 mV (Figure S3, Supporting Information). Subsequently, the template, endowed with a negative surface charge, selectively adsorbed  $Pb^{2+}$  resulting from the hydrolysis of lead acetate trihydrate, followed by the in situ deposition of stable metal complex with the assistance of urotropine. Upon high-temperature calcination, the template transformed into  $TiO_2/PbTiO_3$  with a hollow

structure and a positively charged surface of 31.01 mV (Figure \$3, Supporting Information), enabling the directional adsorption of negatively charged hexakis-[(trimethylsilyl)ethynyl]benzene (HEB-TMS) monomer (-22.34 mV; Figure S3, Supporting Information) and the subsequent in situ growth of GDY<sup>[34]</sup> on its surface. Upon the formation of TiO<sub>2</sub>/PbTiO<sub>3</sub>/GDY, Cs-oleate is introduced as the halide perovskite precursor, enabling the selective in situ transformation of PbTiO3 into CsPbBr3 with the assistance of HBr. In this process, TiO2 and GDY maintain their stability in the presence of HBr (Figures S4, S5, Supporting Information), whereas PbTiO3 is decomposed by HBr to liberate Pb<sup>2+</sup> (Figure S6a, Supporting Information). Given the low formation energy of CsPbBr<sub>3</sub>, the liberated Pb<sup>2+</sup> readily combines with Cs-oleate and Br to form CsPbBr3 in situ, effectively achieving the selective conversion of PbTiO3 to CsPbBr<sub>3</sub> (Figure S6b,c, Supporting Information). This strategy overcomes the deficiencies in the sacrificial template method, ensuring efficient and controllable reactions through precise charge-directed synthesis, thereby providing a reliable approach for the preparation of high-quality ternary heterojunctions.

The morphological evolution of intermediates during the preparation of ternary heterojunctions was analyzed using highresolution scanning electron microscopy (HRSEM) and highresolution transmission electron microscopy (HRTEM). As depicted in Figure 1b, the MIL-125-NH2 template exhibits a nanodisk morphology with a length of approximately 400 nm and a smooth surface. After calcination in an air atmosphere, the original morphology and surface state of MIL-125-NH2 are largely preserved (Figure S7, Supporting Information). Following the in situ growth of a PbTiO<sub>3</sub> layer, the material surface undergoes significantly roughening (Figure 1c). Subsequent reactions result in the uniform coating of GDY on the outer layer, ultimately forming the TiO<sub>2</sub>/PbTiO<sub>3</sub>/GDY composite (Figure 1d). HRTEM image indicates that the in situ conversion of PbTiO<sub>3</sub> to CsPbBr<sub>3</sub> barely alters the sample morphology (Figure 1e), confirming the structural stability of the composite. Energy-dispersive Xray spectroscopy (EDS) mapping measurements were employed to delve deeper into the elemental distribution within the TiO<sub>2</sub>/CsPbBr<sub>3</sub>/GDY composite. As illustrated in Figure 1f-k, Ti, O, Cs, Pb, Br, and C are uniformly dispersed throughout the sample, providing preliminary confirmation for the successful preparation of ternary heterojunction with a hollow structure. After introducing Co active sites during GDY synthesis, the thickness of the outer GDY layer remained nearly constant (approximately 19 nm, Figures S8, S9, Supporting Information), and there was no discernible impact on the sample morphology (Figure S10, Supporting Information). These findings suggest that the introduction of Co does not hinder the preparation of GDY. Notably, replacing the metal source with Bi(NO<sub>3</sub>)<sub>3</sub>·5H<sub>2</sub>O and acid source with HI enables the preparation of ternary heterojunctions TiO<sub>2</sub>/Cs<sub>3</sub>Bi<sub>2</sub>I<sub>9</sub>/GDY (Figure S11, Supporting Information), while replacing the metal source with antimony triacetate can prepare TiO<sub>2</sub>/Cs<sub>3</sub>Sb<sub>2</sub>Br<sub>9</sub>/GDY (Figure S12, Supporting Information). When Bi( $NO_3$ )<sub>3</sub>·5H<sub>2</sub>O serves as the metal source, the introduction of additional AgBr during the conversion process allows for the obtainment of TiO<sub>2</sub>/Cs<sub>2</sub>AgBiBr<sub>6</sub>/GDY (Figure S13, Supporting Information). These results underscore the extensive versatility of the self-templating approach in constructing a diverse range of MHP systems.

16163028, 0, Downloaded from https://advanced.onlinelibrary.wiley.com/doi/10.1002/adfm.202423656 by Tianjin University Of, Wiley Online Library on [03/02/2025]. See the Terms

nditions) on Wiley Online Library for rules of use; OA articles are governed by the applicable Creative Commons License

www.afm-journal.de

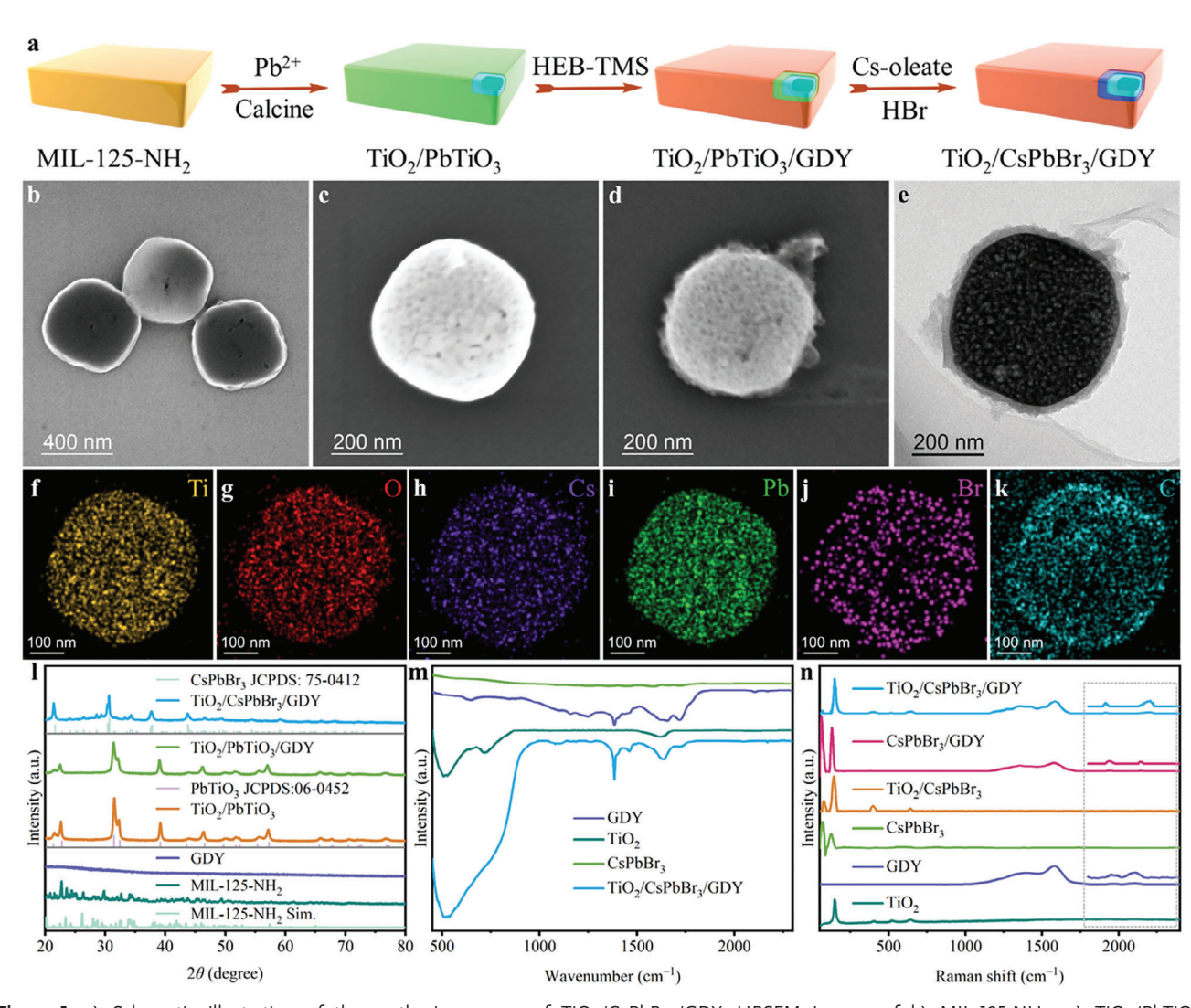


**Figure 1.** a) Schematic illustration of the synthesis process of TiO<sub>2</sub>/CsPbBr<sub>3</sub>/GDY. HRSEM images of b) MIL-125-NH<sub>2</sub>, c) TiO<sub>2</sub>/PbTiO<sub>3</sub>, d) TiO<sub>2</sub>/PbTiO<sub>3</sub>/GDY. e) HRTEM image of TiO<sub>2</sub>/CsPbBr<sub>3</sub>/GDY. f–k) EDS elemental mapping images of TiO<sub>2</sub>/PbTiO<sub>3</sub>/GDY composite: f) Ti, g) O, h) Cs, i) Pb, j) Br, k) C. l) XRD patterns of MIL-125-NH<sub>2</sub>, GDY, TiO<sub>2</sub>/PbTiO<sub>3</sub>, TiO<sub>2</sub>/PbTiO<sub>3</sub>/GDY, and TiO<sub>2</sub>/CsPbBr<sub>3</sub>/GDY. m) FTIR spectra of GDY, TiO<sub>2</sub>, CsPbBr<sub>3</sub>, and TiO<sub>2</sub>/CsPbBr<sub>3</sub>/GDY. n) Raman spectra of TiO<sub>2</sub>, GDY, CsPbBr<sub>3</sub>, TiO<sub>2</sub>/CsPbBr<sub>3</sub>, CsPbBr<sub>3</sub>/GDY, and TiO<sub>2</sub>/CsPbBr<sub>3</sub>/GDY.

Powder X-ray diffraction (PXRD) measurements were further carried out to investigate the structural characteristics of ternary heterojunctions. As shown in Figure 11, the XRD pattern of MIL-125-NH<sub>2</sub> aligns perfectly with the simulated pattern (Figure S14, Supporting Information), [35] indicating the successful synthesis of the template. After calcination in an air atmosphere, the resultant XRD pattern corresponds well with the anatase TiO<sub>2</sub> (Figure S15, Supporting Information, JCPDS: 21–1272), [36] suggesting that the MIL-125-NH2 template can be transformed to TiO<sub>2</sub> through high-temperature calcination. Moreover, when a metal complex is coated onto MIL-125-NH2 and subsequently subjected to high-temperature calcination, the resulting XRD peaks match well with PbTiO<sub>3</sub> (JCPDS: 06-0452),<sup>[37]</sup> which are sufficiently intense and can obscure the peaks associated with TiO<sub>2</sub>. Following the in situ growth of a GDY layer on the PbTiO<sub>3</sub> surface, there are no significant alterations in the XRD peaks, attributed to the weak crystallinity of GDY. Upon the transformation of PbTiO<sub>3</sub>, distinctive peaks corresponding to CsPbBr<sub>3</sub>

(JCPDS: 75–0412) emerge, [38] further affirming the successful fabrication of the  ${\rm TiO_2/CsPbBr_3/GDY}$  composite. The XRD results for the remaining three ternary heterojunctions (Figures S16–S18, Supporting Information) also demonstrate similar regularity, validating that the combination of the self-templating method and the sequential deposition technique enables efficient and controllable synthesis of ternary heterojunctions.

The composition of the TiO<sub>2</sub>/CsPbBr<sub>3</sub>/GDY ternary heterojunction was further examined with the Fourier transform infrared (FTIR) spectroscopy and Raman spectroscopy measurements. As presented in Figure 1m, the pristine CsPbBr<sub>3</sub> lacks IR peaks due to its ionic crystal property, whereas TiO<sub>2</sub> exhibits characteristic vibrational peaks belonging to Ti–O–Ti at 505 and 721 cm<sup>-1</sup>.<sup>[39]</sup> GDY displays multiple IR characteristic peaks, including those at 1384 and 1643 cm<sup>-1</sup> arising from aromatic ring skeletal vibrations, and those at 2101 and 2174 cm<sup>-1</sup> stemming from acetylene bond stretching vibrations.<sup>[40]</sup> It is worth noting that all the aforementioned characteristic peaks are

www.afm-journal.de

16163038, O. Downloaded from https://advanced.onlinelblary.wiley.com/doi/10.1002/adfm.202423566 by Tianjin University Of, Wiley Online Library on [03/0022025]. See the Terms and Conditions (https://onlinelibrary.wiley.com/terms-and-conditions) on Wiley Online Library for rules of use; OA articles are governed by the applicable Creative Commons License and Conditions (https://onlinelibrary.wiley.com/terms-and-conditions) on Wiley Online Library for rules of use; OA articles are governed by the applicable Creative Commons License and Conditions (https://onlinelibrary.wiley.com/terms-and-conditions) on Wiley Online Library for rules of use; OA articles are governed by the applicable Creative Commons License and Conditions (https://onlinelibrary.wiley.com/terms-and-conditions) on Wiley Online Library for rules of use; OA articles are governed by the applicable Creative Commons License and Conditions (https://onlinelibrary.wiley.com/terms-and-conditions) on Wiley Online Library for rules of use; OA articles are governed by the applicable Creative Commons License and Conditions (https://onlinelibrary.wiley.com/terms-and-conditions) on Wiley Online Library for rules of use; OA articles are governed by the applicable Creative Commons License and Conditions (https://onlinelibrary.wiley.com/terms-and-conditions) on Wiley Online Library for rules of use; OA articles are governed by the applicable Creative Commons License and Conditions (https://onlinelibrary.wiley.com/terms-and-conditions) on Wiley Online Library for rules of use; OA articles are governed by the applicable Creative Commons License and Conditions (https://onlinelibrary.wiley.com/terms-and-conditions) on Wiley Online Library for rules of use; OA articles are governed by the applicable Creative Commons License and Conditions (https://onlinelibrary.wiley.com/terms-and-conditions) on Wiley Online Library for rules of use; OA articles are governed by the applicable Creative Commons License and Conditions (https://onlinelibrary.wiley.com/terms-and-conditions) on

detectable in TiO2/CsPbBr3/GDY sample, confirming the inclusion of TiO2 and GDY within the composite. Similarly, corresponding components are identifiable in the IR spectra of TiO<sub>2</sub>/CsPbBr<sub>3</sub> and CsPbBr<sub>3</sub>/GDY binary heterojunctions, as well as other ternary heterojunctions (Figures S19-S22 and Table \$1, Supporting Information). Raman spectra measurement results, exhibited in Figure 1n, can provide more insight into the material composition. Raman signals attributed to symmetric stretching vibrations of O-Ti-O (151 and 643 cm<sup>-1</sup>) and bending vibrations of O-Ti-O<sup>[41]</sup> (404 and 524 cm<sup>-1</sup>) can be detected in TiO2. The characteristic peaks at 70 and 123 cm<sup>-1</sup> of pristine CsPbBr<sub>3</sub> are assigned to [PbBr<sub>6</sub>]<sup>4-</sup> octahedron vibration and Cs<sup>+</sup> ion motion, [42] respectively. Pure GDY displays typical Raman peaks of carbon material, with the G-band at 1575 cm<sup>-1</sup> arising from C-C bond vibrations and the Dband at 1378 cm<sup>-1</sup> induced by intrinsic defects. Notably, Raman peaks at 1957 and 2106 cm<sup>-1</sup> correspond to acetylene bonds  $(C \equiv C)$  and conjugated chains  $(-C \equiv C - C \equiv C -)$ , [43] respectively, indicating the successful synthesis of GDY. In the Raman spectrum of TiO<sub>2</sub>/CsPbBr<sub>3</sub>/GDY, the characteristic peaks of CsPbBr<sub>3</sub>, TiO<sub>2</sub>, and GDY are observed at approximately 75, 150, 399, 517, 647, 1914, and 2194 cm<sup>-1</sup>, respectively, further confirming the composition of the TiO<sub>2</sub>/CsPbBr<sub>3</sub>/GDY ternary heterojunction. Similar conclusions can be drawn from binary heterojunctions (TiO<sub>2</sub>/CsPbBr<sub>3</sub>, CsPbBr<sub>3</sub>/GDY) and other ternary heterojunctions (Figures S23-S25 and Table S2, Supporting Information). Furthermore, inductively coupled plasma-mass spectrometry (ICP-MS) analysis (Figure \$26 and Table \$3, Supporting Information) revealed that the mass percentages of TiO2, MHP  $(MHP = CsPbBr_3, Cs_3Bi_2I_9, Cs_3Sb_2Br_9, or Cs_2AgBiBr_6), and$ GDY in the TiO<sub>2</sub>/MHP/GDY ternary heterojunctions range from 29 to 48%, 40 to 64%, and 7 to 18%, respectively. These findings strongly suggest the successful preparation of the ternary heterojunctions.

## 2.2. Energy Band Structures and Interfacial Interaction of TiO<sub>2</sub>/MHP/GDY Ternary Heterojunction

properties The thermodynamic of components TiO<sub>2</sub>/MHP/GDY ternary heterojunctions were determined using the ultraviolet-visible diffuse reflectance spectroscopy (UV-Vis DRS), ultraviolet photoelectron spectroscopy (UPS), and Mott-Schottky curve measurements. As illustrated in UV-vis DRS spectra (Figure S27, Supporting Information), TiO<sub>2</sub> exhibits an absorption edge at approximately 402 nm, demonstrating a relatively weak photon response in the visible light region, whereas CsPbBr3 displays a strong and broad response up to 548 nm. Consequently, heterojunctions incorporating CsPbBr<sub>3</sub>, namely TiO<sub>2</sub>/CsPbBr<sub>3</sub>/GDY, TiO<sub>2</sub>/CsPbBr<sub>3</sub>, and CsPbBr<sub>3</sub>/GDY, all exhibit robust visible light responses. While GDY possesses full-spectrum absorption, its low coefficient implies that the primary contribution to light-harvesting capability of CsPbBr3-based composites comes from CsPbBr3. Subsequently, the UV-vis DRS data were converted into Tauc plots (Figure S28a-c, Supporting Information) to ascertain the optical band gaps (E<sub>g</sub>) of TiO<sub>2</sub>, CsPbBr<sub>3</sub>, and GDY, which were found to be 3.14, 2.33, and 1.64 eV, respectively. UPS results (Figure 2a) were analyzed to calculate the valence band maximum (VBM)

potentials of TiO<sub>2</sub>, CsPbBr<sub>3</sub>, and GDY to be 2.95, 1.69, and 1.22 V versus the standard hydrogen electrode (vs. SHE), respectively. Additionally, XPS valence band spectra further confirmed the VBM offset of 1.27 eV between TiO<sub>2</sub> and CsPbBr<sub>3</sub>, and of 0.44 eV between CsPbBr<sub>3</sub> and GDY (Figure 2b), indicating a staggered band alignment between TiO<sub>2</sub> and CsPbBr<sub>3</sub>, and a straddling gap band alignment between CsPbBr<sub>3</sub> and GDY (Figure 2c). Mott–Schottky curve measurements (Figure S29a–c, Supporting Information) revealed that the flat-band potentials of TiO<sub>2</sub>, GDY, and CsPbBr<sub>3</sub> are -0.21, -0.41, and -0.66 V (vs. SHE), respectively, which are consistent with the results of UPS and XPS measurements. Comparable thermodynamic information can be obtained from other MHP-based ternary heterojunctions (Figures S28–S33, Supporting Information).

Furthermore, the Fermi levels of TiO2, CsPbBr3, and GDY were determined based on UPS measurements at -5.10, -4.26, and -3.94 eV (relative to the vacuum level), with the band structure diagram portrayed in Figure 2d,I. When the components of the ternary heterojunction are brought into intimate contact, the aforementioned disparities in Fermi levels will initiate spontaneous migration of free electrons, ultimately achieving an equilibrium state among the Fermi energy levels. Specifically, at the interface of TiO<sub>2</sub>/CsPbBr<sub>3</sub>, CsPbBr<sub>3</sub> functions as a donor of free electrons due to its higher Fermi energy level, inducing the transfer of free electrons from CsPbBr<sub>3</sub> to TiO<sub>2</sub>. This process establishes a built-in electric field (BEF, Figure 2d,II) directed from CsPbBr<sub>3</sub> to TiO<sub>2</sub>. It is worth noting that the formation of the BEF is accompanied by the bending of energy bands at the contact interface, specifically manifested as the TiO<sub>2</sub> energy band bending downward and the CsPbBr3 energy band bending upward. Analogously, at the CsPbBr<sub>3</sub>/GDY interface, CsPbBr<sub>3</sub> transforms into the acceptor of free electrons owing to its lower Fermi level, leading to the flow of interfacial electrons from GDY to CsPbBr3 and forming a BEF directed from GDY to CsPbBr<sub>3</sub>, simultaneously causing the energy band of CsPbBr<sub>3</sub> to bend downward and the energy band of GDY to bend upward. Notably, the BEF can further facilitate the directional migration of photogenerated carriers at the heterojunction interface. As depicted in Figure 2d,III, under the influence of BEF and band bending, photogenerated electrons in the conduction band (CB) of TiO<sub>2</sub> are inclined to migrate toward the valence band (VB) of CsPbBr<sub>3</sub>, thereby promoting efficient separation of photogenerated carriers in TiO2/CsPbBr3 heterojunction through a Zscheme charge transfer mechanism. Moreover, the CB and VB of CsPbBr<sub>3</sub> are higher and deeper, respectively, compared to those of GDY, where the direction of the BEF promotes the transfer of photogenerated electrons from the CB of CsPbBr<sub>3</sub> to the CB of GDY. However, the band bending poses a hindrance to the migration of photogenerated holes from CsPbBr3 to GDY. Consequently, the photogenerated carriers at the CsPbBr<sub>3</sub>/GDY interface adhere to a typical type-I heterojunction transfer pathway for separation.

## 2.3. Separation and Transmission of Photogenerated Carriers within TiO<sub>2</sub>/MHP/GDY Ternary Heterojunction

The direction of free electron migration at the heterojunction interface can be confirmed through high-resolution X-ray

16163028, 0, Downloaded from https://advanced.onlinelibrary.wiley.com/doi/10.1002/adfm.202423656 by Tianjin University Of, Wiley Online Library on [03/02/2025]. See the Terms and Conditions (https://onlinelibrary.wiley.com/rerms

and-conditions) on Wiley Online Library for rules of use; OA articles are governed by the applicable Creative Commons License

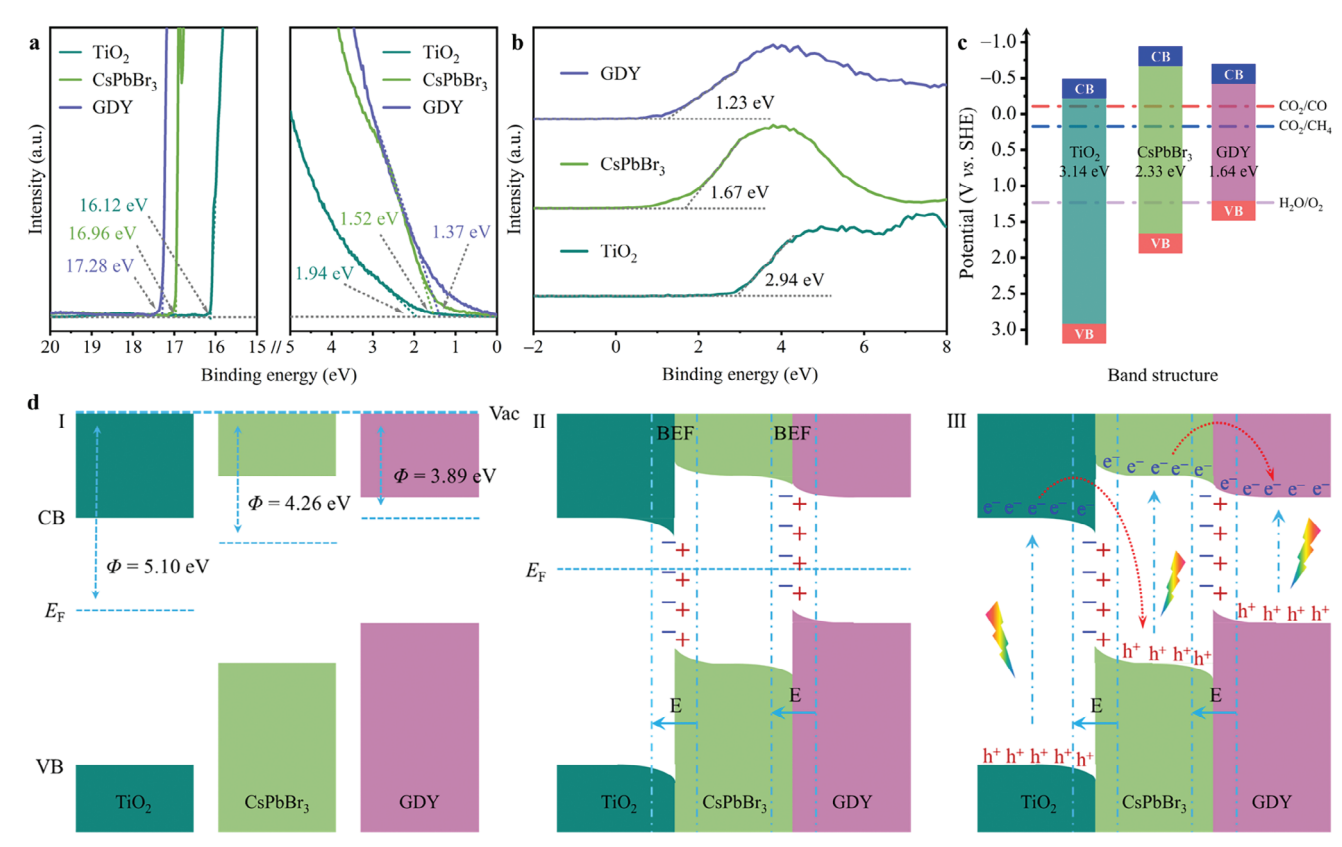


Figure 2. a) UPS spectra, b) XPS valence spectra and c) energy band structure diagrams of  $TiO_2$ ,  $CsPbBr_3$  and GDY. d) Energy band structure and charge transfer in  $TiO_2/CsPbBr_3/GDY$ : Energy band structures of  $TiO_2$ ,  $CsPbBr_3$ , and GDY before I) and after II) contact; III) Charge transfer pathway in  $TiO_2/CsPbBr_3/GDY$  under illumination. Φ denotes the work function, and its value is the negative counterpart of the corresponding Fermi energy level ( $E_F$ ), E denotes the electric field, and the direction of the arrow indicates the direction of the electric field.

photoelectron spectroscopy (XPS) measurements. As displayed in Figure 3a, the characteristic peaks of Cs 3d, Pb 4f, and Br 3d in TiO<sub>2</sub>/CsPbBr<sub>3</sub> shift toward higher binding energies (0.15-0.24 eV) relative to those in CsPbBr<sub>3</sub>, whereas the binding energies of Ti 3d and O 1s in TiO<sub>2</sub>/CsPbBr<sub>3</sub> exhibit a significant shift toward lower values (0.20-0.24 eV) compared to those in TiO<sub>2</sub> (Figure S34, Supporting Information). These changes indicate that free electrons migrate from CsPbBr<sub>3</sub> to TiO<sub>2</sub>. For the CsPbBr<sub>3</sub>/GDY heterojunction (Figure 3b), the binding energies of Cs 3d, Pb 4f, and Br 3d undergo a negative shift (0.11-0.30 eV) compared to CsPbBr3, while C 1s experiences a positive shift (0.26 eV) relative to GDY (Figure \$35, Supporting Information), demonstrating the free electron transfer occurs from GDY to CsPbBr3. These significant variations among element binding energies further suggest the presence of a robust electron coupling effect at the interface upon the formation of heterojunctions, which is pivotal for facilitating the efficient separation of photogenerated carriers.

In-situ XPS measurements were conducted to further validate the migration direction of photogenerated carriers (Figures S36, S37, Supporting Information). As depicted in Figure 3c, the binding energies of Cs 3d, Pb 4f, and Br 3d in  $TiO_2/CsPbBr_3$  decrease by 0.10–0.25 eV under illumination, while those of Ti 3d and O 1s increase by 0.20–0.24 eV. These shifts suggest that photogenerated electrons and holes accumu-

late in CsPbBr<sub>3</sub> and TiO<sub>2</sub>, respectively, thereby confirming that the separation of photogenerated carriers at the TiO<sub>2</sub>/CsPbBr<sub>3</sub> heterojunction interface follows a Z-scheme charge transfer mode. For the CsPbBr<sub>3</sub>/GDY heterojunction (Figure 3d), the binding energies of Cs 3d, Pb 4f, and Br 3d shift positively (0.12–0.49 eV) upon illumination, while the peaks of C 1s shift to lower binding energy (0.24–0.33 eV). These results indicate the enrichment of photogenerated electrons in GDY, further verifying that the separation of photogenerated carriers follows a type-I transfer pathway.

To further elucidate the transfer mechanism of photogenerated carriers, hydroxyl radical (·OH) and furfuryl alcoholoxidized carbon radical (R·) trapping experiments were carried out using 5,5-dimethyl-1-pyrroline-*N*-oxide (DMPO) as the capturing agent. As illustrated in Figure 3e, the absence of ·OH characteristic signal peaks under dark conditions confirms that light illumination is essential for ·OH generation. Additionally, no DMPO—OH signal can be observed with CsPbBr<sub>3</sub> as the photocatalyst, attributed to its insufficient thermodynamic driving force for oxidizing H<sub>2</sub>O into OH (2.40 V vs. SHE). However, the signal intensity of DMPO—OH in TiO<sub>2</sub>/CsPbBr<sub>3</sub> is significantly stronger than that in TiO<sub>2</sub>, suggesting an effective retention of photogenerated holes in the VB of TiO<sub>2</sub> in TiO<sub>2</sub>/CsPbBr<sub>3</sub>, which is indicative of the Z-scheme transfer mechanism of photogenerated carriers at the TiO<sub>2</sub>/CsPbBr<sub>3</sub>

www.afm-journal.de

1616328, 0, Downloaded from https://advanced.onlinelibrary.wiley.com/doi/10.1002/adfm.202423656 by Tianjin University Of, Wiley Online Library on [03:022025]. See the Terms and Conditions (https://onlinelibrary.wiley.com/terms-and-conditions) on Wiley Online Library for rules of use; OA articles are governed by the applicable Creative Commons License and Conditions (https://onlinelibrary.wiley.com/terms-and-conditions) on Wiley Online Library for rules of use; OA articles are governed by the applicable Creative Commons License and Conditions (https://onlinelibrary.wiley.com/terms-and-conditions) on Wiley Online Library for rules of use; OA articles are governed by the applicable Creative Commons License and Conditions (https://onlinelibrary.wiley.com/terms-and-conditions) on Wiley Online Library for rules of use; OA articles are governed by the applicable Creative Commons License and Conditions (https://onlinelibrary.wiley.com/terms-and-conditions) on Wiley Online Library for rules of use; OA articles are governed by the applicable Creative Commons License and Conditions (https://onlinelibrary.wiley.com/terms-and-conditions) on Wiley Online Library for rules of use; OA articles are governed by the applicable Creative Commons License and Conditions (https://onlinelibrary.wiley.com/terms-and-conditions) on Wiley Online Library for rules of use; OA articles are governed by the applicable Creative Commons License and Conditions (https://onlinelibrary.wiley.com/terms-and-conditions) on Wiley Online Library for rules of use; OA articles are governed by the applicable Creative Commons License and Conditions (https://onlinelibrary.wiley.com/terms-and-conditions) on Wiley Online Library for rules of use; OA articles are governed by the applicable Creative Commons License and Conditions (https://onlinelibrary.wiley.com/terms-and-conditions) on Wiley Online Library for rules of use; OA articles are governed by the applicable Creative Commons License and Conditions (https://onlinelibrary.wiley.com/terms-and-conditions) on

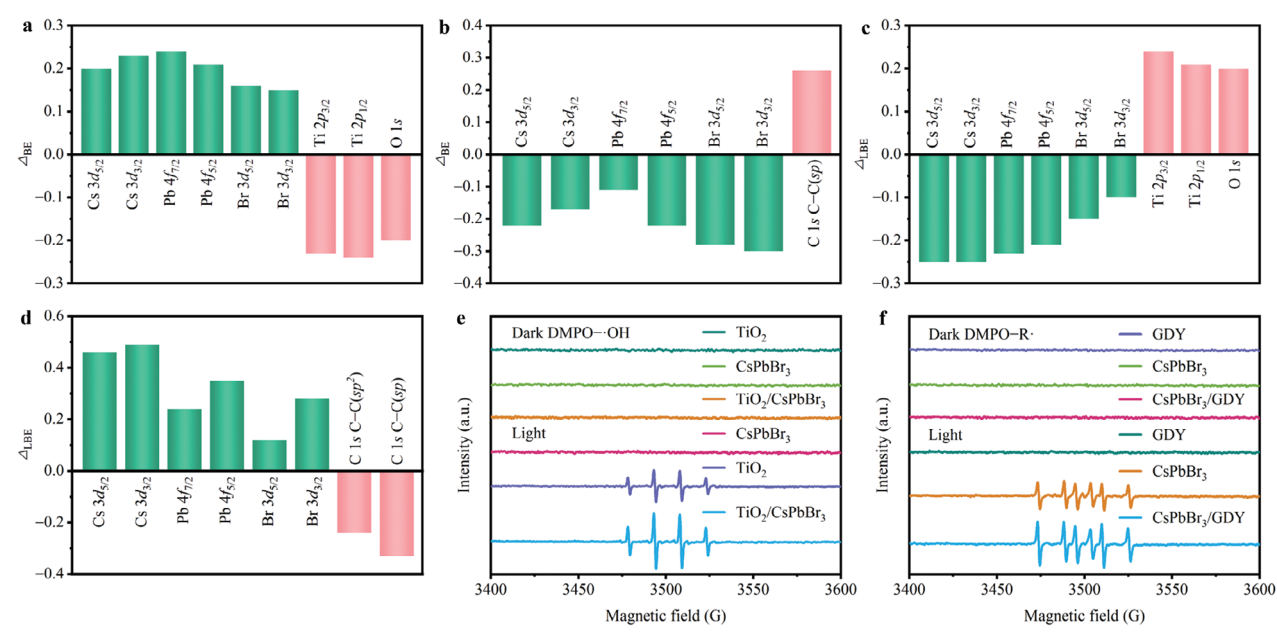


Figure 3. Binding energy shifts ( $\Delta_{BE}$ ) of elements in a) TiO<sub>2</sub>/CsPbBr<sub>3</sub> relative to TiO<sub>2</sub> and CsPbBr<sub>3</sub>, and b) CsPbBr<sub>3</sub>/GDY compared to CsPbBr<sub>3</sub> and GDY under dark derived from high-resolution XPS measurements. Light-induced binding energy shifts ( $\Delta_{LBE}$ ) of elements in c) TiO<sub>2</sub>/CsPbBr<sub>3</sub> and d) CsPbBr<sub>3</sub>/GDY derived from ISI-XPS measurements. e) EPR spectra of DMPO—OH in TiO<sub>2</sub>, CsPbBr<sub>3</sub>, and TiO<sub>2</sub>/CsPbBr<sub>3</sub>. f) EPR spectra of DMPO—Rin CsPbBr<sub>3</sub>, GDY, and CsPbBr<sub>3</sub>/GDY.

interface. Given the weak oxidation abilities of photogenerated holes in CsPbBr3 and GDY, R. radicals produced by the oxidation of furan alcohols were selected as the capture targets to explore the photogenerated carrier transfer mechanism at the CsPbBr<sub>3</sub>/GDY interface. As shown in Figure 3f, none of the samples exhibit the DMPO-R signals under dark conditions. Upon irradiation, the DMPO-R· signals also cannot be observed in GDY, because the photogenerated holes in GDY are unable to drive furfuryl alcohol oxidation (1.44 V vs. SHE).[45] In contrast, CsPbBr<sub>3</sub> demonstrates the capability to oxidize furfuryl alcohol with distinct DMPO-R· signals. Notably, there is a noticeable increase in the DMPO-R· signal upon the formation of the CsPbBr<sub>3</sub>/GDY heterojunction, highlighting the retention and utilization of photogenerated holes in the VB of CsPbBr<sub>3</sub>. This phenomenon suggests the presence of a type-I transfer mechanism at the CsPbBr<sub>3</sub>/GDY interface. Therefore, the TiO2/CsPbBr3/GDY ternary heterojunction exhibits a coexistence of Z-scheme and type-I photogenerated carrier transfer mechanisms.

The dynamics of photogenerated carriers were thoroughly investigated using nanosecond transient absorption spectroscopy measurements. As presented in Figure 4 a–d, negative signals attributed to ground-state bleaching (GSB) of CsPbBr<sub>3</sub> emerge near 520 nm under excitation with a 440 nm laser, indicating the filling of the CB of CsPbBr<sub>3</sub> by excited electrons. Further monitoring of the kinetic recovery traces of the GSB peaks is performed to assess the deactivation processes of photogenerated excitons in different materials (Figure 4e). The multi-exponential fitting result reveals a lifetime of 19.81 ns for the delayed GSB recovery process in CsPbBr<sub>3</sub> (Table S4, Supporting Information). When CsPbBr<sub>3</sub> forms binary heterojunctions with TiO<sub>2</sub> or GDY, the accelerated-GSB recovery processes yield lifetimes of

9.25 ns and 14.23 ns, respectively. Notably, TiO<sub>2</sub>/CsPbBr<sub>3</sub>/GDY exhibits the fastest delayed GSB recovery process with a lifetime of 5.69 ns, suggesting that the dual built-in electric fields significantly enhance the charge transfer efficiency at the heterojunction interface. The photocurrent response (I-t curves) and electrochemical impedance spectroscopy (EIS) tests provide additional evidence supporting the enhancement of charge separation efficiency in the ternary heterojunction. As demonstrated in Figure 4f, the photocurrent intensities of TiO<sub>2</sub>/CsPbBr<sub>3</sub> and CsPbBr<sub>3</sub>/GDY are both higher than those of TiO<sub>2</sub>, CsPbBr<sub>3</sub>, and GDY individually, while TiO2/CsPbBr3/GDY exhibits the highest photocurrent intensity, which validates the promotion effect of the built-in electric fields on interfacial charge separation. Furthermore, the Nyquist plots reveal that the semicircle diameter of TiO<sub>2</sub>/CsPbBr<sub>3</sub>/GDY is significantly smaller compared to those of TiO2, CsPbBr3 and corresponding binary heterojunctions (Figure \$38, Supporting Information). Combined with similar trends observed in other ternary heterojunctions under the same tests (Figures \$39-\$44, Supporting Information), it can be inferred that the dual built-in electric fields in the ternary heterojunction system significantly promote interfacial charge separation.

## 2.4. Photocatalytic CO<sub>2</sub> Reduction Activity and Stability of TiO<sub>2</sub>/MHP/GDY

The activity of artificial photosynthesis was systematically evaluated using a gas–solid reaction setup apparatus with  $\rm CO_2$  and water as raw materials and a xenon lamp as light source (Figure S45, Supporting Information). Gas chromatographic analysis revealed that the primary reduction product of all

1616328, 0, Downloaded from https://advanced.onlinelibarry.wiley.com/doi/10.1002/adfm.202423656 by Tianjin University Of, Wiley Online Library on [03:0022025]. See the Terms and Conditions (https://onlinelibrary.wiley.com/rems-and-conditions) on Wiley Online Library for rules of use; OA articles are governed by the applicable Creative Commons Licrossy

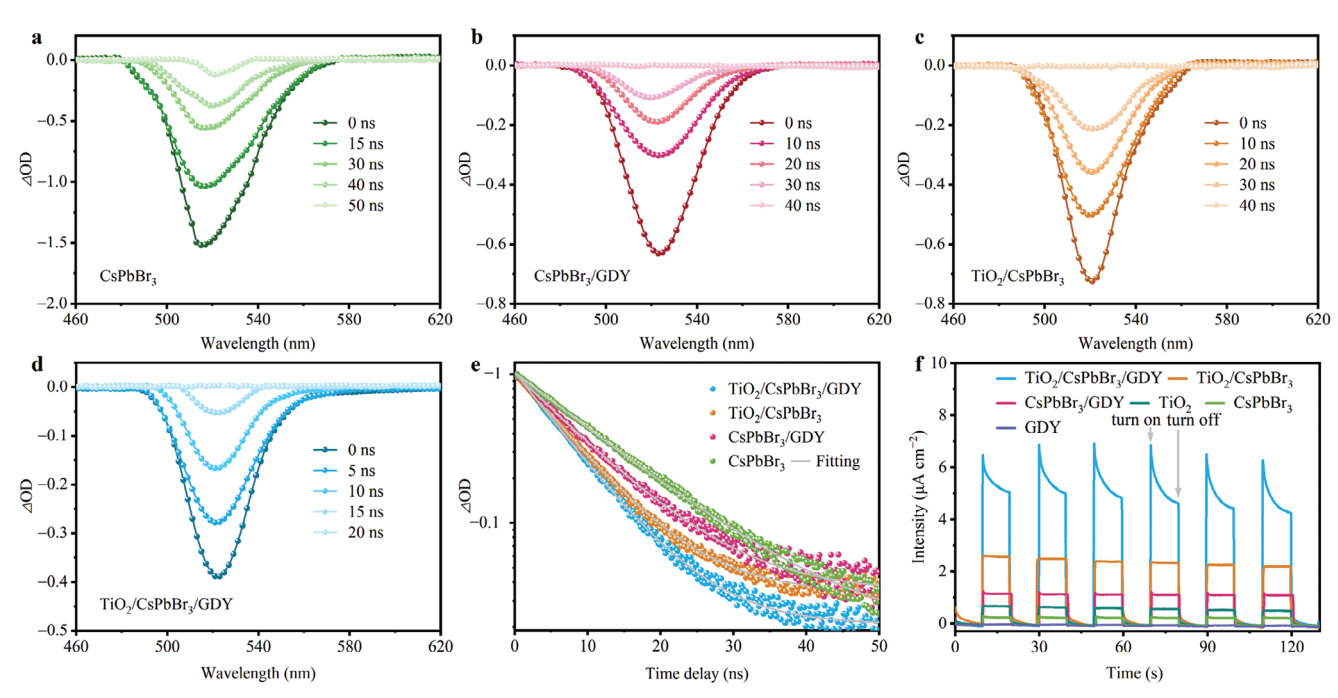


Figure 4. Nanosecond transient absorption (ns-TA) spectroscopies of a) CsPbBr<sub>3</sub>, b) CsPbBr<sub>3</sub>/GDY, c) TiO<sub>2</sub>/CsPbBr<sub>3</sub>, and d) TiO<sub>2</sub>/CsPbBr<sub>3</sub>/GDY at indicated delay times after 440 nm excitation. e) ns-TA kinetic plots of CsPbBr<sub>3</sub>, CsPbBr<sub>3</sub>/GDY, TiO<sub>2</sub>/CsPbBr<sub>3</sub>, and TiO<sub>2</sub>/CsPbBr<sub>3</sub>/GDY monitored at respective GSB peak. f) I-t curves of TiO2, CsPbBr3, GDY, CsPbBr3/GDY, TiO2/CsPbBr3, and TiO2/CsPbBr3/GDY.

samples is CO, accompanied by trace amounts of CH4 and negligible formic acid (GDY was excluded due to its inability to drive the water oxidation reaction for artificial photosynthesis, Table S5 and Figure S46, Supporting Information). As depicted in Figure 5a, TiO<sub>2</sub> with strong H<sub>2</sub>O oxidizing ability achieves a moderate CO yield of 81 µmol g<sup>-1</sup> h<sup>-1</sup> for photocatalytic CO2 reduction. Under the same conditions, CsPbBr3, Cs<sub>3</sub>Bi<sub>2</sub>I<sub>9</sub>, Cs<sub>3</sub>Sb<sub>2</sub>Br<sub>9</sub>, and Cs<sub>2</sub>AgBiBr<sub>6</sub>, with moderate redox potentials and excellent light-absorption abilities, exhibit certain photocatalytic activities with CO yields of 53, 33, 42, and 66 μmol g<sup>-1</sup> h<sup>-1</sup>, respectively. After combining MHP with GDY to form binary heterojunctions, the CO yields of CsPbBr3/GDY, Cs<sub>3</sub>Bi<sub>2</sub>I<sub>9</sub>/GDY, Cs<sub>3</sub>Sb<sub>2</sub>Br<sub>9</sub>/GDY, and Cs<sub>2</sub>AgBiBr<sub>6</sub>/GDY increase to 178, 100, 115, and 101 µmol g<sup>-1</sup> h<sup>-1</sup>, respectively, owing to the improved charge separation efficiency. By integrating MHP with water oxidation catalyst TiO2, both the water oxidation capability and charge separation efficiency are simultaneously enhanced, leading to a further improvement in photocatalytic CO<sub>2</sub> reduction performance. The corresponding binary heterojunctions TiO<sub>2</sub>/CsPbBr<sub>3</sub>, TiO<sub>2</sub>/Cs<sub>3</sub>Bi<sub>2</sub>I<sub>9</sub>, TiO<sub>2</sub>/Cs<sub>3</sub>Sb<sub>2</sub>Br<sub>9</sub>, and TiO2/Cs2AgBiBr6 achieve CO yields of 296, 184, 247, and 238 μmol g<sup>-1</sup> h<sup>-1</sup>, respectively. Notably, all TiO<sub>2</sub>/MHP/GDY ternary heterojunctions demonstrate optimal photocatalytic activities compared to individual MHP and corresponding binary heterojunctions, with CO yields reaching 467, 271, 383, and 303 μmol g<sup>-1</sup> h<sup>-1</sup> for TiO<sub>2</sub>/CsPbBr<sub>3</sub>/GDY, TiO<sub>2</sub>/Cs<sub>3</sub>Bi<sub>2</sub>I<sub>9</sub>/GDY, TiO<sub>2</sub>/Cs<sub>3</sub>Sb<sub>2</sub>Br<sub>9</sub>/GDY, and TiO<sub>2</sub>/Cs<sub>2</sub>AgBiBr<sub>6</sub>/GDY, respectively. This exceptional performance can be attributed to the unique dual BEF at the ternary heterojunction interfaces, which can facilitate efficient separation and transport of photogenerated carriers. Furthermore, the introduction of Co as a cocatalyst in TiO<sub>2</sub>/CsPbBr<sub>3</sub>/GDY ternary heterojunction can further boost the

CO yield to 711 µmol g<sup>-1</sup> h<sup>-1</sup>, accompanied by a photogenerated electron consumption rate of 1825 µmol g<sup>-1</sup> h<sup>-1</sup>, representing a 13-fold increase in CO yield compared to that of single CsPbBr<sub>3</sub> and far exceeding the currently reported halide perovskite-based photocatalysts (Figure 5b).

All of the aforementioned samples were subjected to the longterm photocatalytic test to validate the stability of sandwichstructured ternary heterojunctions, with the exception of pure GDY due to its inherent thermodynamic constraints. As illustrated in Figure 5c-f, the photocatalytic activities of MHPs (CsPbBr<sub>3</sub>, Cs<sub>3</sub>Bi<sub>2</sub>I<sub>9</sub>, Cs<sub>3</sub>Sb<sub>2</sub>Br<sub>9</sub>, and Cs<sub>2</sub>AgBiBr<sub>6</sub>) undergo a significant decline after 24 h and reach a plateau at 72 h, rendering them impractical for sustained photocatalytic CO2 reduction. When MHPs are combined with TiO2 or GDY, the obtained binary heterojunctions can exhibit enhanced photocatalytic activities due to the efficient separation of photogenerated carriers. Nevertheless, binary heterojunctions also exhibit limited stability reaching a plateau in their catalytic performance after 96 h. In contrast, the TiO<sub>2</sub>/MHP/GDY ternary heterojunctions simultaneously demonstrate exceptional photocatalytic activity and stability, maintaining consistent performance over a 200-h photocatalytic process. The virtually unchanged XRD patterns and HRSEM images of post-photocatalytic reactions can further confirm the stability of ternary heterojunctions (Figures S47, S48, Supporting Information). Notably, the XRD characteristic diffraction peaks of MHPs in TiO2/MHP and MHP/GDY binary heterojunctions largely disappear after reaction, accompanied by the emergence of peaks corresponding to TiO2 and GDY (Figures S49-S52, Supporting Information). This may be attributed to the gradual dissociation of MHPs when directly exposed to a water vapor environment, thereby compromising their overall stability.

16163028, 0, Downloaded from https://advanced.onlinelibrary.wiley.com/doi/10.1002/adfm.202423656 by Tianjin University Of, Wiley Online Library on [03/022025]. See the Terms and Conditional Conditio

(https://onlinelibrary.wiley.com/terms-and-conditions) on Wiley Online Library for rules of use; OA articles are governed by the applicable Creative Commons License

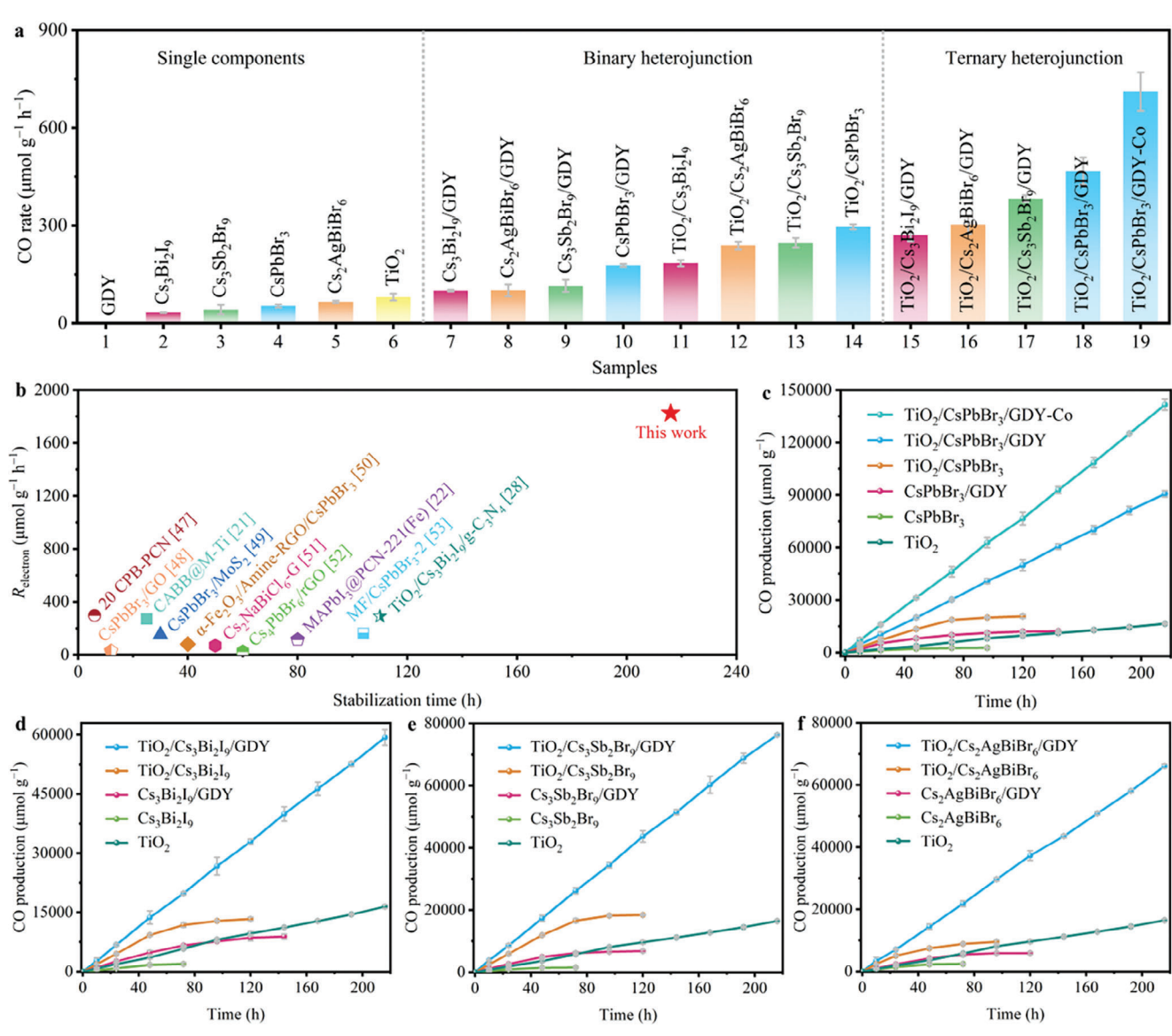


Figure 5. a) The CO generation rate under irradiation of 10 h. b) Comparative data of TiO<sub>2</sub>/CsPbBr<sub>3</sub>/GDY-Co for CO<sub>2</sub> reduction with other reported MHP-based photocatalysts. c-f) CO production during the long-term photocatalytic CO2 reduction with TiO2, MHPs, GDY, MHP/GDY, TiO2/MHP, and  $TiO_2/MHP/GDY$  (MHP = CsPbBr<sub>3</sub>, Cs<sub>3</sub>Bi<sub>2</sub>I<sub>9</sub>, Cs<sub>3</sub>Sb<sub>2</sub>Br<sub>9</sub>, or Cs<sub>2</sub>AgBiBr<sub>6</sub>) as the photocatalysts.

The stability origins of  $TiO_2/MHP/GDY$  (MHP = CsPbBr<sub>3</sub>, Cs<sub>3</sub>Bi<sub>2</sub>I<sub>9</sub>, Cs<sub>3</sub>Sb<sub>2</sub>Br<sub>9</sub>, or Cs<sub>2</sub>AgBiBr<sub>6</sub>) ternary heterojunctions were explored relying on water contact angle measurements. As shown in Figures \$53-\$56 (Supporting Information), TiO<sub>2</sub> exhibits exceptional hydrophilicity with a water contact angle of 13.39°, which is beneficial to water oxidation half-reaction during the photocatalytic process. In contrast, CsPbBr<sub>3</sub>, Cs<sub>3</sub>Bi<sub>2</sub>I<sub>9</sub>, Cs<sub>3</sub>Sb<sub>2</sub>Br<sub>9</sub>, and Cs<sub>2</sub>AgBiBr<sub>6</sub> demonstrate hydrophobicity with contact angles of 46.27°, 44.28°, 28.82°, and 41.54°, respectively. Notably, the pristine GDY shows the highest hydrophobicity with a contact angle of 66.62°, which is conducive to preventing the direct contact between internal MHPs and H2O molecules. The contact angles of TiO<sub>2</sub>/CsPbBr<sub>3</sub>, TiO<sub>2</sub>/Cs<sub>3</sub>Bi<sub>2</sub>I<sub>9</sub>, TiO<sub>2</sub>/Cs<sub>3</sub>Sb<sub>2</sub>Br<sub>9</sub>, and TiO<sub>2</sub>/Cs<sub>2</sub>AgBiBr<sub>6</sub> are 45.17°, 41.23°, 27.89°, and 39.84°, respectively, suggesting that TiO2 is tightly encapsulated by

MHPs. In addition, the contact angles for TiO2/MHP/GDY ternary heterojunctions are nearly identical to those of pure GDY, revealing that the intermediate MHP layers are tightly coated by the outermost GDY layer. It should be noted that although the ternary heterojunction is coated with hydrophobic GDY on its outer layer, the N2 adsorption measurement of the material revealed the presence of 4.5 nm pore diameters within the ternary heterojunction (Figure S57, Supporting Information), ensuring that H<sub>2</sub>O vapor can enter the cavity and combine with TiO2 during the photocatalytic reaction process. Furthermore, physical and chemical adsorption measurements of CO2 for single-components revealed that GDY not only exhibits strong CO2 adsorption capacity but also features a high desorption temperature (Figures \$58 and \$59, Supporting Information), which is favorable for the

16163038, O. Downloaded from https://advanced.onlinelblary.wiley.com/doi/10.1002/adfm.202423566 by Tianjin University Of, Wiley Online Library on [03/0022025]. See the Terms and Conditions (https://onlinelibrary.wiley.com/terms-and-conditions) on Wiley Online Library for rules of use; OA articles are governed by the applicable Creative Commons License and Conditions (https://onlinelibrary.wiley.com/terms-and-conditions) on Wiley Online Library for rules of use; OA articles are governed by the applicable Creative Commons License and Conditions (https://onlinelibrary.wiley.com/terms-and-conditions) on Wiley Online Library for rules of use; OA articles are governed by the applicable Creative Commons License and Conditions (https://onlinelibrary.wiley.com/terms-and-conditions) on Wiley Online Library for rules of use; OA articles are governed by the applicable Creative Commons License and Conditions (https://onlinelibrary.wiley.com/terms-and-conditions) on Wiley Online Library for rules of use; OA articles are governed by the applicable Creative Commons License and Conditions (https://onlinelibrary.wiley.com/terms-and-conditions) on Wiley Online Library for rules of use; OA articles are governed by the applicable Creative Commons License and Conditions (https://onlinelibrary.wiley.com/terms-and-conditions) on Wiley Online Library for rules of use; OA articles are governed by the applicable Creative Commons License and Conditions (https://onlinelibrary.wiley.com/terms-and-conditions) on Wiley Online Library for rules of use; OA articles are governed by the applicable Creative Commons License and Conditions (https://onlinelibrary.wiley.com/terms-and-conditions) on Wiley Online Library for rules of use; OA articles are governed by the applicable Creative Commons License and Conditions (https://onlinelibrary.wiley.com/terms-and-conditions) on Wiley Online Library for rules of use; OA articles are governed by the applicable Creative Commons License and Conditions (https://onlinelibrary.wiley.com/terms-and-conditions) on

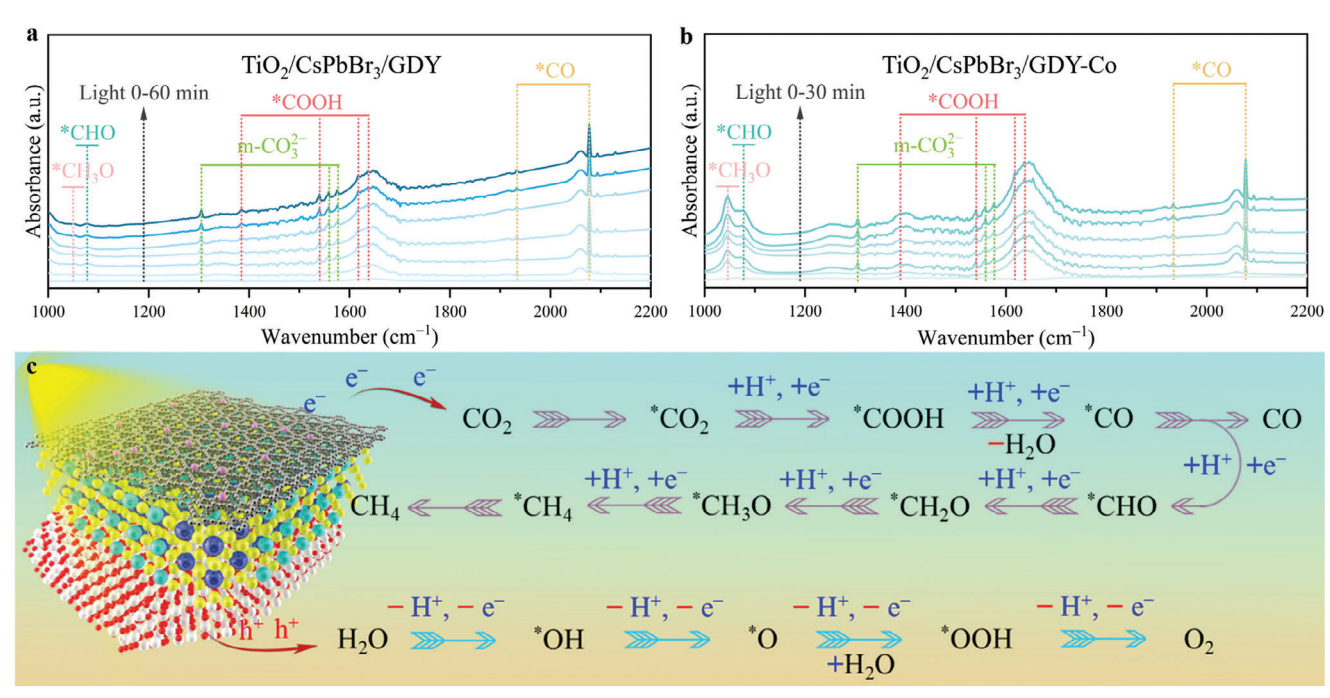


Figure 6. In situ FTIR spectra for photocatalytic CO2 reduction with a) TiO2/CsPbBr3/GDY and b) TiO2/CsPbBr3/GDY-Co as photocatalysts. c) The schematic diagram of proposed reaction pathways of photocatalytic CO<sub>2</sub> reduction over TiO<sub>2</sub>/CsPbBr<sub>3</sub>/GDY-Co.

photocatalytic reduction of CO<sub>2</sub>. These results suggest that the photocatalytic stability and activity of TiO<sub>2</sub>/MHP/GDY ternary heterojunctions are attributed to the sandwich structures. In these structures, MHPs function as light-harvesting units, while TiO<sub>2</sub> efficiently adsorbs H<sub>2</sub>O for water oxidation, and GDY equipped with CO<sub>2</sub> adsorption capacity and hydrophobicity serves as the reduction site. This design can enhance separation efficiency of photogenerated carriers and shield MHPs from direct contact with H<sub>2</sub>O, thereby achieving high photocatalytic activity and stability.

To gain a deeper understanding of the origins of products during the photocatalytic process, a series of control experiments were performed using TiO<sub>2</sub>/CsPbBr<sub>3</sub>/GDY as the photocatalyst (Figure \$60, Supporting Information). The absence of light or catalyst led to the absence of detectable presence of products, indicating that the CO2 reduction process was initiated by light irradiation on the catalyst surface. When CO2 was substituted with Ar and water was omitted, only trace amounts of CO resulting from the decomposition of residues from sample preparation were detected, initially verifying that the photocatalytic products originated from CO<sub>2</sub> and H<sub>2</sub>O. Furthermore, isotope labeling experiments were executed using  ${}^{13}\text{CO}_2$  and  $H_2{}^{18}\text{O}$  as reactants to elucidate the precise origins of products. When <sup>13</sup>CO<sub>2</sub> was used, mass spectrometry analysis (Figure S61a, Supporting Information) revealed signal peaks attributed to  ${}^{13}CH_4$  and  ${}^{13}CO$  at m/z = 17and m/z = 29, respectively, demonstrating that CO and CH<sub>4</sub> were derived from CO<sub>2</sub> photoreduction. When H<sub>2</sub><sup>18</sup>O was employed (Figure S61b, Supporting Information), a signal peak attributed to  $^{18}\text{O}_2$  emerged at m/z = 36, confirming that the stoichiometric amounts of O<sub>2</sub> (Figures S62-S65, Supporting Information) generated during the photocatalytic process indeed originated from water oxidation.

In-situ Fourier transform infrared spectroscopy (in situ FTIR) provides further insight into the reaction mechanism underlying artificial photosynthesis in ternary heterojunction systems. Prior to conducting the formal experiment, the test system was purged with high-purity Ar to eliminate the background interference. Subsequently, CO2 and water vapor were introduced into the system while the light source was activated. Figure 6a displays the results of an in situ FTIR test using TiO<sub>2</sub>/CsPbBr<sub>3</sub>/GDY ternary heterojunction as the photocatalyst. As the light exposure time increases, multiple distinct signal peaks gradually emerge within the wavenumber range of 1000–2200 cm<sup>-1</sup>. Specifically, the signal peaks observed at 1306, 1558, and 1578 cm<sup>-1</sup> are indicative of the characteristic vibrations of monodentate carbonate (m-CO<sub>2</sub><sup>2-</sup>).<sup>[53]</sup> Prominent characteristic signal peaks detected at 1384, 1539, 1618, and 1636 cm<sup>-1</sup> represent \*COOH, [54,55] which is a crucial intermediate during the conversion of CO<sub>2</sub> to CO. Additionally, the presence of \*CO intermediates adsorbed on the catalyst surface is confirmed by signal peaks at 1933 and 2077 cm<sup>-1</sup>. [56,57] Furthermore, signal peaks at 1048 and 1076 cm<sup>-1</sup> correspond to \*CH<sub>3</sub>O and \*CHO, respectively, which are key intermediates in CH<sub>4</sub> formation.<sup>[58]</sup> Under the same conditions, further in situ FTIR measurements were conducted on a sample loaded with the cocatalyst Co (TiO2/CsPbBr3/GDY-Co). As shown in Figure 6b, the incorporation of the co-catalyst modifies the equilibrium time of the intermediates and the intensities of the peaks, but does not alter the types of intermediates or their characteristic peaks, which indicates that the ternary heterojunction photocatalytic reaction pathway remains unchanged upon the addition of the Co co-catalyst.

Based on the aforementioned results, a fundamental reaction pathway for photocatalytic CO2 reduction is proposed in Figure 6c, with TiO<sub>2</sub>/CsPbBr<sub>3</sub>/GDY-Co as an example. Initially,

www.afm-journal.de

16163038, O. Downloaded from https://advanced.onlinelblary.wiley.com/doi/10.1002/adfm.202423566 by Tianjin University Of, Wiley Online Library on [03/0022025]. See the Terms and Conditions (https://onlinelibrary.wiley.com/terms-and-conditions) on Wiley Online Library for rules of use; OA articles are governed by the applicable Creative Commons License and Conditions (https://onlinelibrary.wiley.com/terms-and-conditions) on Wiley Online Library for rules of use; OA articles are governed by the applicable Creative Commons License and Conditions (https://onlinelibrary.wiley.com/terms-and-conditions) on Wiley Online Library for rules of use; OA articles are governed by the applicable Creative Commons License and Conditions (https://onlinelibrary.wiley.com/terms-and-conditions) on Wiley Online Library for rules of use; OA articles are governed by the applicable Creative Commons License and Conditions (https://onlinelibrary.wiley.com/terms-and-conditions) on Wiley Online Library for rules of use; OA articles are governed by the applicable Creative Commons License and Conditions (https://onlinelibrary.wiley.com/terms-and-conditions) on Wiley Online Library for rules of use; OA articles are governed by the applicable Creative Commons License and Conditions (https://onlinelibrary.wiley.com/terms-and-conditions) on Wiley Online Library for rules of use; OA articles are governed by the applicable Creative Commons License and Conditions (https://onlinelibrary.wiley.com/terms-and-conditions) on Wiley Online Library for rules of use; OA articles are governed by the applicable Creative Commons License and Conditions (https://onlinelibrary.wiley.com/terms-and-conditions) on Wiley Online Library for rules of use; OA articles are governed by the applicable Creative Commons License and Conditions (https://onlinelibrary.wiley.com/terms-and-conditions) on Wiley Online Library for rules of use; OA articles are governed by the applicable Creative Commons License and Conditions (https://onlinelibrary.wiley.com/terms-and-conditions) on

Table 1. Chemical reagents involved in TiO<sub>2</sub>/MO<sub>x</sub> preparation process.

Samples	MIL-125-NH <sub>2</sub>	Methenamine	Metal salt
TiO <sub>2</sub> /Bi <sub>2</sub> O <sub>3</sub>	100 mg	20 mg	Bi(NO <sub>3</sub> ) <sub>3</sub> ·5H <sub>2</sub> O 150 mg
TiO <sub>2</sub> /Sb <sub>2</sub> O <sub>4</sub>	100 mg	10 mg	Sb(Ac) <sub>3</sub> 100 mg

 ${\rm TiO_2/CsPbBr_3/GDY\text{-}Co}$  absorbs photons under illumination and generates photogenerated electron-hole pairs. Subsequently, the dual built-in electric field facilitates efficient separation and transport of the photogenerated carriers, resulting in the accumulation of photogenerated electrons primarily in GDY and photogenerated holes mainly in  ${\rm TiO_2}$ . Ultimately, the photogenerated electrons in the CB of GDY trigger the reduction reaction of  ${\rm CO_2}$  through a proton-coupled electron transfer (PCET) pathway, progressively generating intermediates \*COOH and \*CO. The \*CO intermediate either desorbs to from CO or undergoes further PCET transfer reactions to produce  ${\rm CH_4}$ . Concurrently, the photogenerated holes in the VB of  ${\rm TiO_2}$  participate in the oxidation of  ${\rm H_2O}$  to generate  ${\rm O_2}$ , while also providing the necessary protons for the  ${\rm CO_2}$  reduction process.

#### 3. Conclusion

In summary, we have successfully demonstrated a versatile strategy that integrates self-templating with in situ sequential deposition to meticulously prepare a series of MHP-based ternary heterojunctions. The innovative sandwich-like hollow structure not only offers dual-sided protection to the MHP photoactive layers but also ensures intimate contact between the reactant substrates and the respective oxidation and reduction catalysts. Moreover, comprehensive characterizations including UPS, XPS, in situ XPS, EPR, transient absorption spectroscopy and photoelectrochemical measurements have unequivocally confirmed that the generation of the dual-interfacial electric field in the ternary heterojunctions can effectively promote the directional separation of photogenerated carriers, with photogenerated electrons and holes accumulating on the reduction and oxidation catalysts, respectively. Consequently, the prepared MHP-based ternary heterojunctions exhibit remarkable photocatalytic stability in watercontaining systems for over 200 h, and their photocatalytic activities surpass those of both single perovskites and the corresponding binary heterojunctions by a significant margin. Notably, the CsPbBr<sub>3</sub>-based ternary heterojunction demonstrates an impressive electron consumption rate of up to 1824 µmol g<sup>-1</sup> h<sup>-1</sup> for photocatalytic CO<sub>2</sub> reduction coupled with water oxidation, vastly outperforming currently reported halide perovskite-based photocatalysts.

### 4. Experimental Section

Chemicals: Cesium iodide (CsI, 99.9%) and cesium bromide (CsBr, 99.9%) were purchased from Xi'an Polymer Light Technology Corp. Cesium carbonate (Cs<sub>2</sub>CO<sub>3</sub>, 99%) was obtained from J&K. Methanol (99.9%), isopropanol (IPA, 99.5%), ethylene glycol (EG, 98%), acetonitrile (99.8%), titanium isopropoxide ( $Ti(O^iPr)_4$ , 95%), 2-aminoterephthalic acid ( $NH_2$ -BDC, 98%), silver bromide (AgBr, 98%), copper (I) bromide (CuBr, 99%), copper (I) iodide (CuI, 98%),  $N_iN_i$ -dimethylformamide

(DMF, 99.5%), tetrabutylammonium hexafluorophosphate (TBAPF<sub>6</sub>, 98%), oleic acid (OA, AR), and oleylamine (OAm, AR) were all sourced from Aladdin. Lead acetate trihydrate (Pb(Ac)<sub>2</sub>·3H<sub>2</sub>O, 99.5%), 5,5-dimethyl-1-pyrroline *N*-oxide (DMPO, 98%), and furfuryl alcohol (99%) were procured from Adamas-beta. Hydriodic acid (HI, 57 wt%), ethanol (CH<sub>3</sub>CH<sub>2</sub>OH, AR), and antimony acetate (Sb(Ac)<sub>3</sub>, 98%) were procured from Innochem. Bismuth nitrate pentahydrate (Bi(NO<sub>3</sub>)<sub>3</sub>·5H<sub>2</sub>O, 99.9%), <sup>13</sup>CO<sub>2</sub>, and H<sub>2</sub><sup>18</sup>O were obtained from Energy Chemical. Methenamine (C<sub>6</sub>H<sub>12</sub>N<sub>4</sub>, 99%) was purchased from Sinopharm Chemical Reagent Co. Ltd. Hexakis-[(trimethylsilyl)ethynyl]benzene (HEB-TMS, 97%) was purchased from LEYAN. Hydrobromic acid (HBr, 47%) was purchased from TCI. Cobalt bromide (CoBr<sub>2</sub>, 99.99%) was purchased from Alfa. All chemicals were commercially available and used without further purification.

Preparation of MIL-125-NH $_2$ : MIL-125-NH $_2$  was synthesized by modifying the previously reported method. [59] First, NH $_2$ -BDC (840 mg, 4.65 mmol) was dissolved in 60 mL of a mixture of DMF and methanol ( $V_{\rm DMF}$ : $V_{\rm methanol}=8:2$ ) and stirred for 30 min. After the solution turned clear, Ti(O'Pr) $_4$  (900 µL, 3 mmol) was added dropwise and the mixture was stirred for another 10 min. Finally, the resulting mixture was placed into a 100 mL Teflon-lined stainless autoclave and stored at 150 °C for 16 h. After cooling to room temperature, the product was collected by centrifugation, washed with DMF and ethanol, and finally dried to obtain MIL-125-NH $_2$ .

Preparation of  $TiO_2/PbTiO_3$ : As-prepared MIL-125-NH $_2$  (100 mg), ethanol (20 mL), EG (5 mL), methenamine (20 mg) and Pb(Ac) $_2\cdot 3$ H $_2$ O (100 mg) were first added into a beaker. Subsequently, the mixture was stirred for 10 h at 85 °C in a water bath followed by centrifugation, and the obtained precipitate was washed with deionized water and ethanol. Eventually, the precipitate was annealed at 450 °C for 3 h to get  $TiO_2/PbTiO_3$ . For details on the chemicals used in the preparation of other binary composite materials, refer to **Table 1**.

Preparation of TiO<sub>2</sub>/PbTiO<sub>3</sub>/GDY and TiO<sub>2</sub>/PbTiO<sub>3</sub>/GDY-Co: TiO<sub>2</sub>/PbTiO<sub>3</sub>/GDY was synthesized based on the Glaser-Eglinton coupling reaction reported in the literature.<sup>[34]</sup> Typically, TiO<sub>2</sub>/PbTiO<sub>3</sub> (10 mg), CuBr (2 mg), HEB-TMS (2 mg) were first dispersed in DMF (5 mL). After ultrasonic treatment for 10 min, the mixture was stirred at 60 °C for 24 h. Subsequently, the precipitate was collected by centrifugation and further washed with DMF and ethanol to obtain TiO<sub>2</sub>/PbTiO<sub>3</sub>/GDY. Cobalt ions were introduced by adding 0.2 mg of CoBr<sub>2</sub> during the synthesis process. The preparation process for other ternary composite materials (TiO<sub>2</sub>/Bi<sub>2</sub>O<sub>3</sub>/GDY and TiO<sub>2</sub>/Sb<sub>2</sub>O<sub>4</sub>/GDY) is similar, involving only the substitution of different binary composites.

Preparation of TiO2/CsPbBr3/GDY and TiO2/CsPbBr3/GDY-Co: First, Cs2CO3 (200 mg) and OA (30 mL) were added into a round-bottom flask (50 mL), and the mixture was degassed under Ar flow at 140 °C for 1 h before being heated to 180 °C for 30 min to form the Cs-oleate. Second, the obtained Cs-oleate was added into IPA (170 mL) to prepare a Cs-oleate precursor solution (1 mg mL $^{-1}$ ). Subsequently, the Cs-oleate precursor solution (4 mL), TiO2/PbTiO3/GDY (10 mg), OAm (100 μL), and IPA (1 mL) were added to three-necked round-bottom flask and sonicated for 15 min. Ultimately, HBr (50 μL) was added to the reaction system and stirred for 30 min followed by washing with IPA three times. For the synthesis of TiO2/CsPbBr3/GDY-Co, the Cs-oleate precursor solution (4 mL), TiO2/PbTiO3/GDY-Co (10 mg), OAm (100 μL), and IPA (1 mL) were added to three-necked round-bottom flask and sonicated for 15 min. Ultimately, HBr (50 μL) was added to the reaction system and stirred for 30 min followed by washing with IPA three times.

www.advancedsciencenews.com

www.afm-journal.de

16163028, 0, Downloaded from https://advanced.onlinelibrary.wiley.com/doi/10.1002/adfm.202423656 by Tianjin University Of, Wiley Online Library on [03/02/2025]. See the Terms and Conditions

nditions) on Wiley Online Library for rules of use; OA articles are governed by the applicable Creative Commons License

FUNCTIONAL MATERIALS

Preparation of  $TiO_2/Cs_3Bi_2I_9/GDY$  and  $TiO_2/Cs_3Sb_2Br_9/GDY$ : First,  $TiO_2/Bi_2O_3/GDY$  (10 mg) and CsI (20 mg) were dispersed in methanol (5 mL) until a uniform dispersion was achieved by sonication. Subsequently, HI (100  $\mu$ L) was rapidly poured into the above mixture solution under vigorous stirring, and the mixture was continuously stirred for 2 h. Finally, the product was separated by centrifugation and washed with IPA three times. The  $TiO_2/Cs_3Sb_2Br_9/GDY$  ternary heterojunction was prepared in a similar process, except that CsI and HI are replaced with CsBr (15 mg) and HBr (100  $\mu$ L), respectively.

Preparation of  $TiO_2/Cs_2AgBiBr_6/GDY$ : First, CsBr (18 mg), AgBr (8 mg), methanol (2 mL) and HBr (3 mL) were mixed in a round-bottom flask. The solid reactants were then completely dissolved by ultrasonic treatment. Subsequently,  $TiO_2/Bi_2O_3/GDY$  (10 mg) was introduced into the aforementioned mixture and stirred for 30 min. After the reaction, the precipitate was collected by centrifugation and washed with IPA to obtain the desired  $TiO_2/Cs_2AgBiBr_6/GDY$ .

## **Supporting Information**

Supporting Information is available from the Wiley Online Library or from the author.

### Acknowledgements

This work was financially supported by the National Key R&D Program of China (2022YFA1502902), NSFC (22475152, U21A20286, and 22305214), and the 111 Project of China.

### **Conflict of Interest**

The authors declare no conflict of interest.

#### **Data Availability Statement**

The data that support the findings of this study are available from the corresponding author upon reasonable request.

### Keywords

CO<sub>2</sub> reduction, metal halide perovskite, photocatalysis, self-template, ternary heterojunction

Received: December 2, 2024 Revised: January 4, 2025 Published online:

- [1] J. Lv, J. Xie, A. G. A. Mohamed, X. Zhang, Y. Feng, L. Jiao, E. Zhou, D. Yuan, Y. Wang, Nat. Rev. Chem. 2023, 7, 91.
- [2] M. Bonchio, J. Bonin, O. Ishitani, T.-B. Lu, T. Morikawa, A. J. Morris, E. Reisner, D. Sarkar, F. M. Toma, M. Robert, Nat. Catal. 2023, 6, 657.
- [3] J. Fu, K. Jiang, X. Qiu, J. Yu, M. Liu, Mater. Today 2020, 32, 222.
- [4] W. Liu, L. Cao, W. Cheng, Y. Cao, X. Liu, W. Zhang, X. Mou, L. Jin, X. Zheng, W. Che, Q. Liu, T. Yao, S. We, Angew. Chem., Int. Ed. 2017, 56, 9312.
- [5] K. Sun, Y. Huang, Q. Wang, W. Zhao, X. Zheng, J. Jiang, H.-L. Jiang, J. Am. Chem. Soc. 2024, 146, 3241.
- [6] J. Wang, H. Zhang, Y. Nian, Y. Chen, H. Cheng, C. Yang, Y. Han, X. Tan, J. Ye, T. Yu, Adv. Funct. Mater. 2024, 34, 2406549.

- [7] F. Li, L. Cheng, J. Fan, Q. Xiang, J. Mater. Chem. A 2021, 9, 23765.
- [8] J. Shamsi, A. S. Urban, M. Imran, L. D. Trizio, L. Manna, Chem. Rev. 2019, 119, 3296.
- [9] Z.-Y. Chen, N.-Y. Huang, Q. Xu, Coord. Chem. Rev. 2023, 481, 215031.
- [10] P. Chen, W.-J. Ong, Z. Shi, N. Li, Adv. Funct. Mater. 2020, 30, 1909667.
- [11] M. L. Davies, Joule 2020, 4, 1626.
- [12] F. Du, X. Liu, J. Liao, D. Yu, N. Zhang, Y. Chen, C. Liang, S. Yang, G. Fang, Adv. Funct. Mater. 2024, 34, 2312175.
- [13] H. Zhao, K. Kordas, S. Ojala, J. Mater. Chem. A 2023, 11, 22656.
- [14] K. Bienkowski, R. Solarska, L. Trinh, J. Widera-Kalinowska, B. Al-Anesi, M. Liu, G. K. Grandhi, P. Vivo, B. Oral, B. Yılmaz, R. Yıldırım, ACS Catal. 2024, 14, 6603.
- [15] J.-S. Zhao, Y.-F. Mu, L.-Y. Wu, Z.-M. Luo, L. Velasco, M. Sauvan, D. Moonshiram, J.-W. Wang, M. Zhang, T.-B. Lu, Angew. Chem., Int. Ed. 2024, 63, 202401344.
- [16] Y.-F. Mu, H.-L. Liu, M.-R. Zhang, H.-J. Wang, M. Zhang, T.-B. Lu, J. Energy Chem. 2023, 77, 317.
- [17] J. Zhu, L. Zhou, Y. Zhu, J. Huang, L. Hou, J. Shen, S. Dai, C. Li, Small 2022. 18. 2104399.
- [18] J. Gao, X. Qian, Q. Wei, Z. Chen, C. Liu, W. Wang, J. Chen, X. Chen, Y. Liu, G. Wei, J. Colloid Interface Sci. 2022, 623, 974.
- [19] Y.-F. Xu, X.-D. Wang, J.-F. Liao, B.-X. Chen, H.-Y. Chen, D.-B. Kuang, Adv. Mater. Interfaces 2018, 5, 1801015.
- [20] Q.-M. Sun, J.-J. Xu, F.-F. Tao, W. Ye, C. Zhou, J.-H. He, J.-M. Lu, Angew. Chem., Int. Ed. 2022, 61, 202200872.
- [21] L. Ding, F. Bai, B. Borjigin, Y. Li, H. Li, X. Wang, Chem. Eng. J. 2022, 446, 137102.
- [22] L.-Y. Wu, Y.-F. Mu, X.-X. Guo, W. Zhang, Z.-M. Zhang, M. Zhang, T.-B. Lu, Angew. Chem., Int. Ed. 2019, 58, 9491.
- [23] V. Andrei, G. M. Ucoski, C. Pornrungroj, C. Uswachoke, Q. Wang, D. S. Achilleos, H. Kasap, K. P. Sokol, R. A. Jagt, H. Lu, T. Lawson, A. Wagner, S. D. Pike, D. S. Wright, R. L. Z. Hoye, J. L. MacManus-Driscoll, H. J. Joyce, R. H. Friend, E. Reisner, *Nature* 2022, 608, 518.
- [24] J. Zhuang, J. Wang, F. Yan, Nano-Micro Lett. 2023, 15, 84.
- [25] Q.-Q. Chu, Z. Sun, D. Wang, B. Cheng, H. Wang, C.-P. Wong, B. Fang, Matter 2023, 6, 3838.
- [26] M. Heydarian, M. Heydarian, P. Schygulla, S. K. Reichmuth, A. J. Bett, J. Hohl-Ebinger, F. Schindler, M. Hermle, M. C. Schubert, P. S. C. Schulze, J. Borchert, S. W. Glunz, *Energy Environ. Sci.* 2024, 17, 1781.
- [27] Y.-X. Feng, K. Su, Z.-L. Liu, S.-X. Yuan, Y.-F. Mu, M. Zhang, T.-B. Lu, Appl. Catal. B Environ. Energy 2024, 347, 123821.
- [28] B. Kim, W. Lee, S. Lim, Appl. Surf. Sci. 2024, 657, 159829.
- [29] Y. Ma, X. Yi, S. Wang, T. Li, B. Tan, C. Chen, T. Majima, E. R. Waclawik, H. Zhu, J. Wang, Nat. Commun. 2022, 13, 1400.
- [30] J. Zhu, X. F. Lu, D. Luan, X. W. (David) Lou, Angew. Chem., Int. Ed. 2024, 63, 202408846.
- [31] Z.-X. Cai, Z.-L. Wang, J. Kim, Y. Yamauchi, Adv. Mater. 2019, 31, 1804903.
- [32] X. Liu, G. Verma, Z. Chen, B. Hu, Q. Huang, H. Yang, S. Ma, X. Wang, Innovation 2022, 3, 100281.
- [33] Y. Chang, H. Huang, T. Yang, L. Wang, H. Zhu, C. Zhong, J. Colloid Interface Sci. 2021, 599, 785.
- [34] J. Li, X. Han, D. Wang, L. Zhu, M.-H. Ha-Thi, T. Pino, J. Arbiol, L.-Z. Wu, M. N. Ghazzal, Angew. Chem., Int. Ed. 2022, 61, 202210242.
- [35] C. Li, Z. Yu, K. Cui, J. R. Schmidt, D. S. Sholl, R. P. Lively, J. Phys. Chem. C 2022, 126, 21414.
- [36] Z.-W. Wei, H.-J. Wang, C. Zhang, K. Xu, X.-L. Lu, T.-B. Lu, Angew. Chem., Int. Ed. 2021, 60, 16622.
- [37] Y. Feng, M. Xu, H. Liu, W. Li, H. Li, Z. Bian, Nano Energy 2020, 73, 104768
- [38] H. Lu, Y. Tang, L. Rao, Z. Li, X. Ding, C. Song, B. Yu, Nanotechnology 2019, 30, 295603.
- [39] Z. Hu, K. Li, X. Wu, N. Wang, X. Li, Q. Li, L. Li, K. Lv, Appl. Catal. B Environ. 2019, 256, 117860.



www.advancedsciencenews.com



www.afm-journal.de

16163028, 0, Downloaded from https://advanced.onlinelibrary.wiley.com/doi/10.1002/adfm.202423656 by Tianjin University Of, Wiley Online Library on [03/02/2025]. See the Terms

and-conditions) on Wiley Online Library for rules

of use; OA articles

are

governed by the applicable Creative Commons License

- [40] G. Li, Y. Li, H. Liu, Y. Guo, Y. Li, D. Zhu, Chem. Commun. 2010, 46, 3256.
- [41] F. Tian, Y. Zhang, J. Zhang, C. Pan, J. Phys. Chem. C 2012, 116, 7515.
- [42] H. Chen, A. Guo, J. Zhu, L. Cheng, Q. Wang, Appl. Surf. Sci. 2019, 465, 656.
- [43] K. Su, G.-X. Dong, W. Zhang, Z.-L. Liu, M. Zhang, T.-B. Lu, ACS Appl. Mater. Interfaces 2020, 12, 50464.
- [44] Z. Jiang, W. Wan, H. Li, S. Yuan, H. Zhao, P. K. Wong, Adv. Mater. 2018, 30, 1706108.
- [45] W. Zhang, C.-C. Song, J.-W. Wang, S.-T. Cai, M.-Y. Gao, Y.-X. Feng, T.-B. Lu, Chin. J. Catal. 2023, 52, 176.
- [46] M. Ou, W. Tu, S. Yin, W. Xing, S. Wu, H. Wang, S. Wan, Q. Zhong, R. Xu, Angew. Chem., Int. Ed. 2018, 57, 13570.
- [47] Y.-F. Xu, M.-Z. Yang, B.-X. Chen, X.-D. Wang, H.-Y. Chen, D.-B. Kuang, C.-Y. Su, J. Am. Chem. Soc. 2017, 139, 5660.
- [48] X. Wang, J. He, L. Mao, X. Cai, C. Sun, M. Zhu, Chem. Eng. J. 2021, 416, 128077.
- [49] Y. Jiang, J.-F. Liao, H.-Y. Chen, H.-H. Zhang, J.-Y. Li, X.-D. Wang, D.-B. Kuang, Chem 2020, 6, 766.

- [50] J. Pi, X. Jia, Z. Long, S. Yang, H. Wu, D. Zhou, Q. Wang, H. Zheng, Y. Yang, J. Zhang, J. Qiu, Adv. Energy Mater. 2022, 12, 2202074.
- [51] X. Wang, K. Li, J. He, J. Yang, F. Dong, W. Mai, M. Zhu, Nano Energy 2020, 78, 105388.
- [52] Q. Chen, Y. Ma, L. Wang, X. Lan, J. Shi, Sol. RRL 2021, 5, 2000755.
- [53] Y. Zhang, X. Zhi, J. R. Harmer, H. Xu, K. Davey, J. Ran, S.-Z. Qiao, Angew. Chem., Int. Ed. 2022, 61, 202212355.
- [54] S. Barman, A. Singh, F. A. Rahimi, T. K. Maji, J. Am. Chem. Soc. 2021, 143, 16284.
- [55] G. Zhou, J. Yang, X. Zhu, Q. Li, Q. Yu, W. El-alami, C. Wang, Y. She, J. Qian, H. Xu, H. Li, J. Energy Chem. 2020, 49, 89.
- [56] N. Li, X.-P. Zhai, B. Ma, H.-J. Zhang, M.-J. Xiao, Q. Wang, H.-L. Zhang, J. Mater. Chem. A 2023, 11, 4020.
- [57] Y. Wang, K. Wang, J. Meng, C. Ban, Y. Duan, Y. Feng, S. Jing, J. Ma, D. Yu, L. Gan, X. Zhou, *Nano Energy* 2023, 109, 108305.
- [58] X. Li, Y. Sun, J. Xu, Y. Shao, J. Wu, X. Xu, Y. Pan, H. Ju, J. Zhu, Y. Xie, Nat. Energy 2019, 4, 690.
- [59] Z. Yang, X. Xu, X. Liang, C. Lei, Y. Cui, W. Wu, Y. Yang, Z. Zhang, Z. Lei, Appl. Catal. B Environ. 2017, 205, 42.